CrossMark

Multiwavelength Emission from Galactic Jets: The Case of the Microquasar SS433

Takahiro Sudoh[1] , Yoshiyuki Inoue[2,3] , and Dmitry Khangulyan[4]

[1] Department of Astronomy, University of Tokyo, Hongo, Tokyo 113-0033, Japan; sudoh@astron.s.u-tokyo.ac.jp
[2] Interdisciplinary Theoretical & Mathematical Science Program (iTHEMS), RIKEN, 2-1 Hirosawa, Saitama 351-0198, Japan
[3] Kavli Institute for the Physics and Mathematics of the Universe (WPI), UTIAS, The University of Tokyo, Kashiwa, Chiba 277-8583, Japan
[4] Department of Physics, Rikkyo University, Nishi-Ikebukuro 3-34-1, Toshima-ku, Tokyo 171-8501, Japan

Abstract

SS433 is a Galactic microquasar with powerful jets, where very-high-energy particles are produced. We study particle acceleration in the jets of SS433 through the use of recent multiwavelength data from radio to TeV gamma-ray. We first present a general framework for the particle acceleration, cooling, and transport in relativistic jets. We then apply this to two X-ray knots in the jets of SS433, focusing on leptonic emission. Our detailed treatment of particle transport and evolution produces substantially different predictions from previous papers. For both regions, our model can account for the multiwavelength data except for the GeV data. This suggests that GeV emission is mostly from different regions and/or mechanisms. We find that the acceleration process should be efficient, which could be realized by diffusive shock acceleration close to the Bohm limit. Provided that protons are accelerated at the same efficiency as electrons, our results imply that SS433 is a PeVatron, i.e., can accelerate protons beyond a PeV. Future hard X-ray and MeV gamma-ray observations can critically test our models by detecting the spectral turnover or cutoff.

Unified Astronomy Thesaurus concepts: Gamma-ray astronomy (628); Nonthermal radiation sources (1119); Relativistic jets (1390); X-ray astronomy (1810); Binary stars (154); Cosmic ray sources (328); Astrophysical black holes (98)

1. Introduction

Microquasar SS433 is a binary system consisting of a compact object (most likely a black hole) and a supergiant star (e.g., Hillwig et al. 2004; Hillwig & Gies 2008; Kubota et al. 2010; Cherepashchuk et al. 2019), which is believed to feed a supercritical accretion disk (e.g., Begelman et al. 2006; Medvedev & Fabrika 2010; Cherepashchuk et al. 2013). Thanks to its relative proximity (5.5 kpc, Blundell & Bowler 2004; Lockman et al. 2007) and a number of unique features, this object has been intensively studied for decades, though many aspects remain mysterious (see Fabrika 2004 for a review). A particularly striking feature is a pair of jets, which are launched almost perpendicular to the line of sight, and show periodic precession and nodding motion (Abell & Margon 1979; Fabian & Rees 1979). They are mildly relativistic ($v = 0.26c$, where c is the speed of light) and have plenty of power ($\sim 10^{39}$ erg s^{-1}, e.g., Marshall et al. 2002; Brinkmann et al. 2005). The jets interact with the surrounding nebula W50, believed to be a supernova remnant (e.g., Dubner et al. 1998; Green 2004).

Recently, the HAWC collaboration has reported the detection of $\gtrsim 25$ TeV gamma rays from the jets of SS433 (Abeysekara et al. 2018). The locations of the gamma-ray emission are ~ 30 pc away from the binary both in the eastern and western side and coincide with nonthermal X-ray emitting regions (Watson et al. 1983; Yamauchi et al. 1994; Brinkmann et al. 1996; Safi-Harb & Ögelman 1997; Safi-Harb & Petre 1999). This indicates that these regions are plausible sites for the acceleration of high-energy (HE) particles. SS433/W50 has also been detected with *Fermi*/Large Area Telescope (*Fermi*/LAT; Bordas et al. 2015; Bordas et al. 2017; Rasul et al. 2019; Sun et al. 2019; Xing et al. 2019), though the origin of the HE gamma-ray emission (>100 MeV) remains unclear. Imaging atmospheric Cherenkov telescopes have not yet

detected this system either from the jets nor from the binary in the very-high-energy (VHE) regime (>100 GeV, Kar 2017; Ahnen et al. 2018).

Multiwavelength emission from the jets of SS433 provides us with valuable opportunities to study the acceleration of particles in astrophysical jets in great detail. There are a number of theoretical studies on the nonthermal emission in microquasars (e.g., Atoyan & Aharonian 1999; Heinz & Sunyaev 2002; Romero et al. 2003; Bosch-Ramon et al. 2006; Gupta et al. 2006; Orellana et al. 2007; Perucho & Bosch-Ramon 2008; Reynoso et al. 2008; Romero & Vila 2008; Bordas et al. 2009; Vila & Romero 2010; Zdziarski et al. 2014; Pepe et al. 2015; Khangulyan et al. 2018; Molina & Bosch-Ramon 2018; Zhang et al. 2018; Reynoso & Carulli 2019). The detection of TeV gamma rays from SS433 provides new important constraints on emission models. However, there are only a few studies that utilize new observational data, and the results remain somewhat controversial. Abeysekara et al. (2018) focused on the eastern region and concluded that the radio, X-ray, and VHE data can be well fit with leptonic models. On the other hand, Xing et al. (2019) studied the western region and argued that leptonic models have difficulties in explaining the radio and X-ray data simultaneously. Because both papers adopt simple models, where particles are continuously injected throughout the source lifetime (~ 20 kyr, Zealey et al. 1980; Goodall et al. 2011a) and cooled only via radiative loss, a new theoretical study with more detailed physical consideration is needed to uncover the origin of the emissions from the jets of SS433.

Here, we study the nonthermal emission from the SS433 jets in the light of recent multiwavelength observations. We aim to assess the validity of leptonic models, to examine the efficiency of particle acceleration and processes responsible for that, and to study prospects for future observations. Going beyond prior
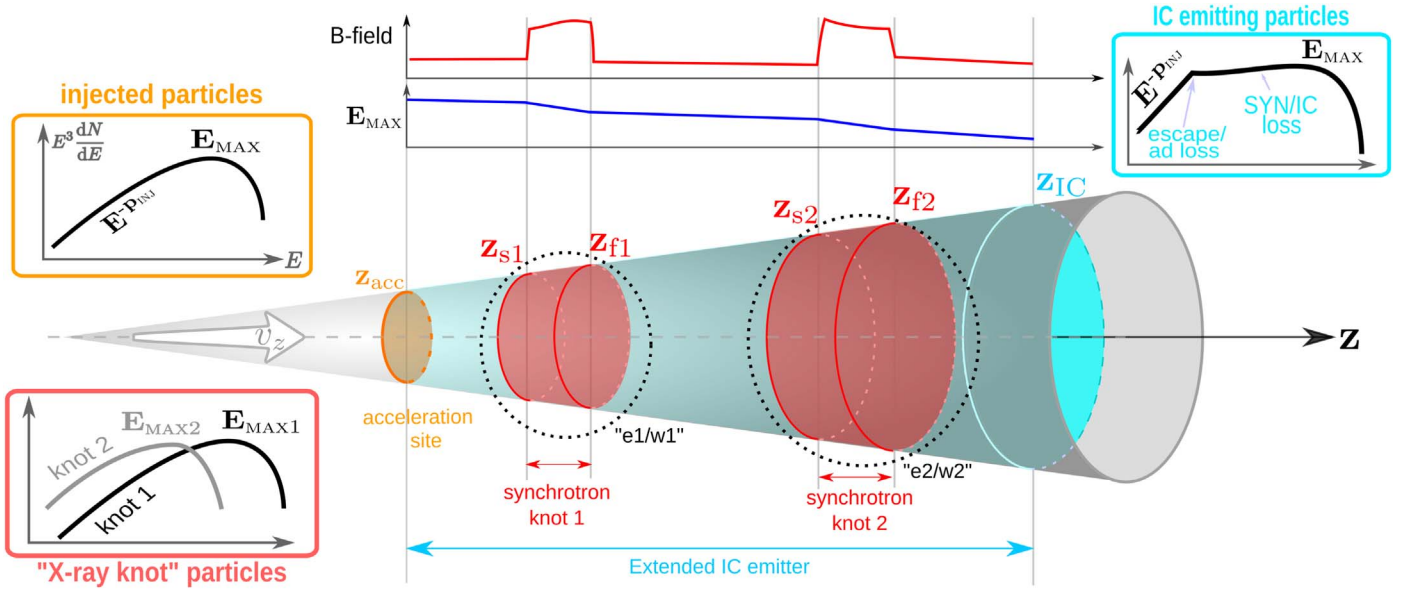
Figure 1. Schematic illustration of our model for the jet, emission regions, and expected energy distributions of particles.

work noted above, we consider the spatial distribution of emission along the jet and include adiabatic loss due to the jet expansion.

In Figure 1, we schematically show how an astrophysical jet and the emission sites can be modeled. Galactic and extragalactic jets often contain multiple compact emitting regions ("knots"), which may appear distinct due to various reasons. For example, an X-ray knot may correspond to the region with a locally enhanced magnetic field. In the case of SS433, the jets are launched to both eastern and western sides, each of which contains multiple X-ray knots, and in Figure 1 we only show one side of the jet. Further description of Figure 1 is presented in Section 2.5. We mainly analyze the emission from the innermost knots ("e1" and "w1") to compare results with Abeysekara et al. (2018) and Xing et al. (2019), but also address the emission of different regions qualitatively. Also, we consider the case where the acceleration site matches the onset of the innermost knot. We only study leptonic emission, as hadronic emission is already disfavored as the dominant source of TeV gamma rays from SS433 (Abeysekara et al. 2018). However, the inferred electron acceleration efficiency can also have implications for the production of HE protons.

In Section 2, we present a general model for the particle evolution and emission in relativistic jets. In Section 3, we briefly review the observational properties of SS433. In Section 4, we compare our model predictions with the multiwavelength data from the two X-ray knots. In Section 5, we study the morphology of the emission regions. In Section 6, we note limitations to our results. In Section 7, we summarize our results and discuss further implications.

2. Physical Conditions in a Relativistic Jet

2.1. Energetics

Let us consider a relativistic jet of total power $L_{\rm jet}$. The jet radius depends on the coordinate on the jet axis, denoted as z: $R = R(z)$. The jet energy flux is

$$L_{\rm jet} = \pi R^2(z) w \Gamma^2 v_z, \tag{1}$$

where w is the plasma enthalpy per unit volume, v_z is the jet velocity, and $\Gamma = [1 - (v_z/c)^2]^{-\frac{1}{2}}$ is the bulk Lorentz factor. The enthalpy is carried by protons, leptons, and magnetic fields. We assume that the jet power is distributed by dimensionless fractions ξ_p, ξ_e, and $\xi_{\rm B}$ for each component, such that $\xi_p + \xi_e + \xi_{\rm B} = 1$. The proton contribution determines the mass flux:

$$\dot{M}_{\rm jet} = \pi R^2(z) n_p m_p \Gamma v_z. \tag{2}$$

The magnetic field is necessary for the acceleration of particles and the production of synchrotron radiation. Its energy is carried as the Poynting flux:

$$L_{\rm B} = \frac{v_z \Gamma^2 R^2(z) B^2(z)}{4}, \tag{3}$$

where B is the strength of the magnetic field in the plasma comoving frame, and we assume that it is perpendicular to the jet velocity in the above expression for simplicity. From this, we can express B as

$$B(z) = \frac{2}{\Gamma R(z)} \sqrt{\frac{\xi_{\rm B} L_{\rm jet}}{v_z}}. \tag{4}$$

2.2. Particle Acceleration

The process responsible for the acceleration of nonthermal particles in the microquasar jet is not certain. We characterize it by an efficiency $\eta_{\rm acc} (>1)$. The time required for a particle to gain energy E is

$$\tau_{\rm acc} = \eta_{\rm acc} \frac{r_L}{c}, \tag{5}$$

where $r_L = E/(eB)$ is the relativistic gyroradius and e is the elementary charge.

The confinement of particles in the acceleration region implies the following condition:

$$R(z) > \sqrt{6 \tau_{\rm acc} D}, \tag{6}$$

where D is the particle diffusion coefficient and we assume a three-dimensional case. This is similar to the Hillas criterion ($r_L < R$, Hillas 1984). We introduce a parameter $\eta_g(>1)$, known as gyrofactor, and characterize the spatial diffusion as $D = \eta_g D_{\mathrm{Bohm}}$, where $D_{\mathrm{Bohm}} = c r_L/3$ is the Bohm diffusion coefficient. Combining above equations, we obtain

$$R(z)B(z) > \frac{E}{e}\sqrt{2\eta_{\mathrm{acc}}\eta_g}, \qquad (7)$$

which constrains the maximum energy of particles that can be confined in the jet during the acceleration process:

$$E < E_{\mathrm{max}}^{\mathrm{con}} = \frac{e}{\Gamma}\sqrt{\frac{2\xi_B L_{\mathrm{jet}}}{v_z \eta_{\mathrm{acc}}\eta_g}}. \qquad (8)$$

The confinement condition is not the only constraint, as the particle acceleration is also limited by energy losses. In this work, we consider emission from electrons. Thus, in the highest-energy regime, the synchrotron cooling may provide the dominant loss mechanism. The synchrotron cooling time is

$$\tau_{\mathrm{syn}} = \frac{3(m_e c^2)^2}{4c\sigma_T E}\left(\frac{B^2}{8\pi}\right)^{-1}, \qquad (9)$$

where σ_T is the Thomson cross section and m_e is the electron mass. The acceleration is possible while it proceeds on a shorter timescale than cooling, $\tau_{\mathrm{acc}} < \tau_{\mathrm{syn}}$, which sets the maximum energy of particles:

$$E < E_{\mathrm{max}}^{\mathrm{syn}} = m_e c^2 \sqrt{\frac{6\pi e}{\sigma_T \eta_{\mathrm{acc}} B}}. \qquad (10)$$

The magnetic field used above should be evaluated in the acceleration site, which can, in principle, differ from that in the emission region (see Figure 1).

2.3. Particle Cooling

Accelerated particles are subject to energy losses due to adiabatic and radiative cooling. The adiabatic loss rate due to the expansion of the jet is

$$\dot{\gamma}_{\mathrm{ad}} = \frac{\gamma}{3}\frac{d\ln\rho}{d\tau} = -\frac{2}{3}\frac{\Gamma v_z}{R(z)}\frac{\partial R}{\partial z}\gamma, \qquad (11)$$

where ρ is number density of matter in the jet, and we assume that the jet speed v_z is constant (thus, ρR^2 is also constant).

The radiative losses for HE electrons are dominated by the synchrotron emission and inverse Compton (IC) scattering. The synchrotron loss rate is

$$\dot{\gamma}_{\mathrm{syn}} = -\frac{4c\sigma_T\gamma^2}{3m_e c^2}\left(\frac{B_{\mathrm{eff}}^2}{8\pi}\right), \qquad (12)$$

where the magnetic field B_{eff} corresponds to the averaged effective field strength. If the magnetic field strength is constant, B, and the pitch angles between the particle velocity and the magnetic field are random, we should use $B_{\mathrm{eff}}^2 = 2B^2/3$. In more general cases, the field strength may have spatial variation within the emission region probably due to magnetic turbulence (e.g., Bykov et al. 2012; Kelner et al. 2013; Derishev & Aharonian 2019). Then, the magnetic field distribution function is needed to obtain B_{eff}.

To describe the IC losses, we need to consider the contributions from all relevant photon fields. A precise treatment requires integration over photon energy and angular distribution, which can be complex. Fortunately, the photon energy distribution is often described by a blackbody-like spectrum, where the photon field is defined by its temperature T and energy density u_{rad} or, equivalently, by the dilution coefficient:

$$\kappa = \frac{15\hbar^3 c^3 u_{\mathrm{rad}}}{\pi^2 k_B^4 T^4}, \qquad (13)$$

where k_B is the Boltzmann constant and $\hbar = h/(2\pi)$ is the Dirac constant. If the jet bulk Lorentz factor is small and the target photon is blackbody-like, the simple approximate description obtained by Khangulyan et al. (2014) is applicable for the energy losses including Klein–Nishina effect:

$$\dot{\gamma}_{\mathrm{ic}} = -\frac{3\sigma_T k_B^2 T^2 m_e c^2 \kappa}{4\pi^2 \hbar^3 c} G_{\mathrm{iso}}^{(0)}\left(4\gamma\frac{k_B T}{m_e c^2}\right)g_{\mathrm{iso}}\left(4\gamma\frac{k_B T}{m_e c^2}\right), \quad (14)$$

where the function $G_{\mathrm{iso}}^{(0)}(u)$ and $g_{\mathrm{iso}}(u)$ are given in their Equations (38) and (20), respectively. In more general cases, when the bulk Lorentz factor is large or the photon direction deviates from isotropic, we need to perform integration over the photon angular distribution.

2.4. Particle Evolution

The distribution of nonthermal particles in the jet can be described with the energy–spatial density, n, as $dN = n d\gamma dz$, where dN is the number of particles. The density is described by the relativistic transport equation (see Webb 1989; Vaidya et al. 2018 for details):

$$\Gamma\left(\frac{\partial}{\partial t} + v_z\frac{\partial}{\partial z}\right)n(\gamma, t, z)$$
$$+ \frac{\partial}{\partial\gamma}[\dot{\gamma}_{\mathrm{cool}}(\gamma, t, z)n(\gamma, t, z)] = \dot{q}_{\mathrm{inj}}(\gamma, t, z), \qquad (15)$$

where $\dot{q}_{\mathrm{inj}}dz$ is the rate of particle injection in the jet segment $(z, z + dz)$. We assume that nonthermal particles are accelerated at a specific coordinate $z = z_{\mathrm{acc}}$:

$$\dot{q}_{\mathrm{inj}}(\gamma, t, z) = \dot{q}_0(\gamma, t)\delta_D(z - z_{\mathrm{acc}}), \qquad (16)$$

where δ_D is the Dirac function. For simplicity, we consider the case where the cooling rate $\dot{\gamma}_{\mathrm{cool}}$ depends only on γ. Then, the solution of the transport equation is obtained analytically:

$$n(\gamma, z, t) = \frac{\dot{\gamma}_{\mathrm{cool}}(\tilde{\gamma})}{\Gamma v_z \dot{\gamma}_{\mathrm{cool}}(\gamma)}\dot{q}_0(\tilde{\gamma}, \tilde{t})\mathcal{H}(z - z_{\mathrm{acc}}), \qquad (17)$$

where $\tilde{t} = t - (z - z_{\mathrm{acc}})/v_z$, $\mathcal{H}$ is the Heaviside function and $\tilde{\gamma}$ is an energy parameter determined by

$$z - z_{\mathrm{acc}} = \Gamma v_z \int_\gamma^{\tilde{\gamma}} \frac{d\hat{\gamma}}{-\dot{\gamma}_{\mathrm{cool}}(\hat{\gamma})}. \qquad (18)$$

To calculate the total emission from a specific region along the jet, we integrate the particle distribution over the emitting region ($z_s < z < z_f$):

$$\frac{dN}{d\gamma} = \int_{z_s}^{z_f} dz\, n(\gamma, z, t). \qquad (19)$$

Assuming a steady injection ($\partial \dot{q}_0 / \partial t = 0$), we obtain

$$\frac{dN}{d\gamma} = \frac{1}{\Gamma v_z \dot{\gamma}_{\rm cool}(\gamma)} \int_{z_s}^{z_f} dz \dot{\gamma}_{\rm cool}(\tilde{\gamma}) \dot{q}_0(\tilde{\gamma}), \qquad (20)$$

where $\tilde{\gamma}$ is determined by $z_{\rm acc}$, z, and γ via Equation (18). As we focus on compact knots much smaller than the jet length, $(z_f - z_s) \ll z_f$, we assume that the change in radius is also small, $R(z_f) - R(z_s) \ll R(z_f)$, and evaluate $\dot{\gamma}_{\rm ad}$ and $B(z)$ at $z_I = (z_s + z_f)/2$ to omit the z dependence. Also, we assume that the onset of emission region matches the acceleration site, i.e., $z_{\rm acc} = z_s$.

We assume that particles are accelerated to a power-law energy distribution above $\gamma > \gamma_{\rm min}$ with an exponential cutoff:

$$\dot{q}_0(\gamma) \propto \gamma^{-p_{\rm inj}} \exp(-\gamma/\gamma_{\rm max}) \mathcal{H}(\gamma - \gamma_{\rm min}), \qquad (21)$$

where $\gamma_{\rm max}$ is defined from either Equations (8) or (10).

The power carried by relativistic electrons, $\xi_e L_{\rm jet}$, defines the normalization for the energy distribution:

$$\int_{\gamma_{\rm min}}^{\gamma_{\rm max}} \dot{q}_0(\gamma) \gamma d\gamma = \frac{\xi_e L_{\rm jet}}{m_e c^2 \Gamma^2}. \qquad (22)$$

The value of $\gamma_{\rm min}$ is theoretically related to the energy scale where thermal particles are injected into the acceleration processes. This is extensively studied, but still contains large uncertainties (Amano & Hoshino 2012). We assume a minimum electron energy of 1 GeV. Smaller values of $\gamma_{\rm min}$ would increase the total electron energy required in the spectral fitting but do not alter the shape in the energy range of interest.

Once the electron distribution is determined, we calculate the spectral energy distribution from synchrotron and IC radiation in jet frame, taking into account Klein–Nishina effect (e.g., Blumenthal & Gould 1970; Aharonian et al. 2010; Khangulyan et al. 2014). In more general cases when the bulk Lorentz factor is large, we need to apply relativistic transformations to obtain the spectral energy distribution in the observer frame.

2.5. Qualitative Description of the Particle Spectrum

If the particle cooling time is shorter than the advection time, $\tau_{\rm adv} = (z_f - z_s)/(\Gamma v_z)$, the particle spectrum is described by the standard formula (fast cooling regime):

$$\frac{dN}{d\gamma} \simeq \frac{1}{\dot{\gamma}(\gamma)} \int_\gamma^\infty d\tilde{\gamma} \dot{q}(\tilde{\gamma}). \qquad (23)$$

For a power-law injection with $p_{\rm inj} \simeq 2$, this expression reduces to $dN/d\gamma \simeq \dot{q}(\gamma) \tau_{\rm cool}$. In this regime, the electron energy distribution has a break, at which the particle power-law index is changed by 1, caused by the transition from the synchrotron/Thomson to adiabatic cooling (or uncooled). This is qualitatively shown in Figure 1 labeled as "IC emitting particles."

If we consider emission from compact knots, the advection time may be shorter than the cooling time (slow cooling regime). The particle spectrum is described by

$$\frac{dN}{d\gamma} \simeq \dot{q}(\gamma) \tau_{\rm adv}, \qquad (24)$$

which has a shape similar to the injection spectrum. This is qualitatively shown in Figure 1 labeled as "knot 1." In knots further away from the acceleration site, the particle number per unit energy per unit volume remains unchanged at lower energies. However, the cutoff energy in the spectrum may be reduced due to the cooling; this can be directly seen from Equation (18). This is qualitatively shown in Figure 1 labeled as "knot 2."

2.6. Knot Size

Observations in radio, optical, or X-rays often reveal knots in Galactic and extragalactic jets. In general, their size may be determined by either of the following factors: (i) nonthermal cooling; (ii) size of the jet region with an enhanced magnetic field; or (iii) size of the region where the acceleration takes place or time elapsed since the onset of the acceleration process.

If the knot size is determined by the particle cooling, the energy requirements for the acceleration process are minimal and the spectral slopes are typical ones for the fast cooling regime. If the particle acceleration occurs at a specific location in the jet, advective particle transport determines the knot size, s, as $s \simeq \Gamma v_z \tau_{\rm cool}(E)$. If synchrotron losses are dominant, the cooling time depends on the particle energy, $\tau_{\rm cool} \propto 1/E$. The synchrotron emission frequency ω and particle energy relate as $E \propto \sqrt{\omega/B}$, and thus the knot size should depend on the photon frequency as $s \propto 1/\sqrt{\omega}$. If adiabatic losses dominate the particle cooling, the knot size does not depend on the particle energy. Adiabatic cooling generally does not produce compact knots, except for specific hydrodynamic structures of the jet. For example, for a constant velocity jet and conical or parabolic shape, it operates on a scale comparable to the jet length.

The synchrotron emissivity is sensitive to the magnetic field strength. If some portion of the jet has an enhanced magnetic field, it may appear as a compact, bright spot. This may result in different morphology for the synchrotron and IC emission (see Figure 1).

The acceleration does not necessarily proceed at a specific point in the laboratory frame, and may be associated with a fluid element. In this case, the knot size depends on the size of the acceleration site and the typical diffusion length, $\lambda_{\rm D}$. Because $\lambda_{\rm D} \propto \sqrt{\tau}$, the size of the knot should have a weaker dependence on the photon frequency as compared to the synchrotron cooling scenario.

There can also be a possibility that the acceleration has started recently and the knot size is limited by the advection distance since the moment of onset of the acceleration. This would produce a gradual increase in the knot size with time. However, this may be difficult to observe on a reasonable timescale.

3. Application to SS433

3.1. Properties of SS433 Jets

Observations of the jets of SS433 provide necessary parameters for the formalism presented in Section 2. We adopt a distance of $d = 5.5$ kpc, which is obtained from deep radio imaging (Blundell & Bowler 2004). Long-term observations and kinematic modelings of the Doppler-shifted emission lines place tight constraints on the jet precession model. They yield a jet speed of $v_z = 0.26c$ (Margon & Anderson 1989; Eikenberry et al. 2001), or equivalently, $\Gamma = 1.04$. Because this is only mildly relativistic, we do not take relativistic effects into account. Models of the jet emission indicate that the mass-loss rate at the jet base is $\dot{M}_{\rm jet} \gtrsim 10^{-7} M_\odot \, {\rm yr}^{-1}$, which leads to the

estimates for the kinetic energy without rest mass energy, $(\Gamma - 1)\dot{M}_{\mathrm{jet}}c^2$, which typically fall within $\sim(0.2\text{–}5) \times 10^{39}$ erg s^{-1}. (e.g., Kotani et al. 1996; Brinkmann & Kawai 2000; Marshall et al. 2002; Brinkmann et al. 2005; Medvedev & Fabrika 2010; Waisberg et al. 2019). Because estimates for the total jet power L_{jet} have uncertainties, instead of using ξ_e and ξ_B, we will leave $L_e(=\xi_e L_{\mathrm{jet}})$ and $L_B(=\xi_B L_{\mathrm{jet}})$ as free parameters. We adopt the jet kinetic energy of 10^{39} erg s^{-1} at the jet base, and assume that part of this is dissipated to L_e and L_B, i.e., we keep $L_e + L_B < 10^{39}$ erg s^{-1}.

We assume a conical jet, and parameterize the radius with the opening angle α_j as $R(z) = z\alpha_j$. We adopt a radius of $R(z_I) = 6$ pc, comparable to the size of X-ray emission (Safi-Harb & Ögelman 1997). With this parameterization, Equation (11) reduces to

$$-\dot{\gamma}_{\mathrm{ad}} = \frac{2}{3}\frac{\Gamma v_z}{z}\gamma. \tag{25}$$

The photon field is also a necessary ingredient as a target for the IC scattering. We adopt a Galactic radiation field composed of the cosmic microwave background $(T, u_{\mathrm{rad}}) = (2.7\,\mathrm{K}, 0.26\,\mathrm{eV\,cm}^{-3})$, far-infrared $(30\,\mathrm{K}, 0.6\,\mathrm{eV\,cm}^{-3})$, optical/near-infrared $(5000\,\mathrm{K}, 0.6\,\mathrm{eV\,cm}^{-3})$, and ultraviolet $(20000\,\mathrm{K}, 0.6\,\mathrm{eV\,cm}^{-3})$ photons (Popescu et al. 2017; Porter et al. 2017).

The accretion disk in SS433 has a high bolometric luminosity of $L_{\mathrm{bol}} \simeq 10^{40}$ erg s^{-1} and temperature of $T \simeq 10^5$ K (e.g., Antokhina & Cherepashchuk 1987; Begelman et al. 2006). At the knot regions, the energy density of this disk emission is $u_{\mathrm{rad}} \sim 2$ eV cm^{-3}. However, due to the Klein–Nishina effect, the contribution of this component to the IC spectrum is suppressed above $E_\gamma \gtrsim 10$ GeV. Furthermore, even in the Thomson regime, the emissivity of IC emission scales as $L_{\mathrm{IC}} \propto u_{\mathrm{rad}} T^{(\alpha_e - 3)/2}$, where α_e is the spectral index for the electron distribution (Blumenthal & Gould 1970; Aharonian et al. 1997). As we focus on the knot emission, where electrons are in slow cooling regime and have a hard spectrum, the contribution of the disk photons is subdominant compared to the cosmic microwave background. Thus, in what follows, we do not consider this component. We have verified that this emission contributes negligibly to the detected GeV emission unless we adopt unrealistically high-energy density of $u_{\mathrm{rad}} \sim 100$ eV cm^{-3}.

3.2. Multiwavelength Observations Toward X-Ray Knots

The jets from SS433 have been intensively studied with multiwavelength observations. Based on ROSAT and *Advanced Satellite for Cosmology and Astrophysics* (*ASCA*) X-ray data, Safi-Harb & Ögelman (1997) defined distinct circular regions to east (e1, e2, e3) and west (w1, w2) from the binary. Combining *RXTE* data, the emission from e1 is fit with a single power law of $\Gamma_{\mathrm{ph}} = 1.43 \pm 0.1$ (Safi-Harb & Petre 1999), while e2 is a broken power-law spectrum of $\Gamma_{\mathrm{ph},1} = 1.6^{+0.2}_{-0.3}$ and $\Gamma_{\mathrm{ph},2} = 2.6^{+0.6}_{-0.3}$ with a break at $E_b = 3.0^{+0.6}_{-0.5}$ keV (Safi-Harb & Ögelman 1997). The eastern jet is also observed with *XMM-Newton* by Brinkmann et al. (2007). They found $\Gamma_{\mathrm{ph}} = 2.17 \pm 0.02$ for the brightest region in the eastern jet and $\Gamma_{\mathrm{ph}} = 1.85 \pm 0.06$ for a region closer to the binary. These regions are not identical to e2 and e1, though they overlap. It should be noted that the derived Galactic column density in Safi-Harb & Ögelman (1997) is $N_{\mathrm{H}} = 1.2^{+0.8}_{-0.5} \times 10^{21}$ cm^{-2} for e2, while it is $N_{\mathrm{H}} = 5.6^{+0.1}_{-0.1} \times 10^{21}$ cm^{-2} in Brinkmann et al. (2007). This may cause differences in the derived photon index.

In the VHE regime, the H.E.S.S., MAGIC, and VERITAS collaborations placed upper limits on the flux from knots (e1, e2, w1, w2) and termination region (e3) (Kar 2017; Ahnen et al. 2018) following the definitions in Safi-Harb & Ögelman (1997). The HAWC collaboration reported the detection of VHE photons ($\gtrsim 25$ TeV) from regions that coincide with X-ray knots. The eastern emission is seemingly radiated from a region spanning over e1 and e2, and the western component is likely centered at w1, though both are not yet well localized.

In the radio band, fluxes from the knot regions are uncertain. The termination region (e3) is prominent in radio images and well-correlated with X-ray intensity maps. However, the knots, e1, e2, and w1, are not resolved in the 2.7 GHz map by the Effelsberg telescope (Geldzahler et al. 1980) nor in the recent 150 MHz map by LOFAR (Broderick et al. 2018). This suggests that the contribution from X-ray knots to the observed radio intensity may be subdominant, and the radio fluxes should be treated as upper limits. Radio spectral index measurements would provide useful constraints on the spectral shape of nonthermal electrons. Downes et al. (1986) produced a radio spectral index map utilizing 1.7, 2.7, and 4.75 GHz data. However, the X-ray knots are not well localized also in this map.

In contrast to other wavelengths, recent results in the HE regime are controversial. Bordas et al. (2015) suggests that emission from nonthermal protons accelerated in the jet termination shock best explains the emission detected with *Fermi*/LAT. The analysis by Xing et al. (2019) suggests a one-sided jet morphology toward the w1 region. While these papers indicate no signature of time variation, Rasul et al. (2019) reports $\sim 3\sigma$ evidence for temporal modulation of the gamma-ray emission with the precession period of the jet, which would indicate core origin (see also Molina & Bosch-Ramon 2018). Sun et al. (2019) suggest that the morphology of the GeV emission is consistent with originating from the radio nebula W50. The spectrum and morphology are somewhat different from each other. Thus, it is difficult at this point to clearly define the HE gamma-ray flux from the X-ray knots.

Further observations are needed to quantify the multi-wavelength properties of the X-ray knots better. Here, we constrain our model parameters by using the same data set for radio, X-ray, and VHE emission as in Abeysekara et al. (2018) and Xing et al. (2019), aiming at comparing model predictions with them. We also compare our model spectra with the GeV data from Bordas et al. (2017), Xing et al. (2019), Rasul et al. (2019), and Sun et al. (2019), which are not used in the model fitting.

We adopt the definition of e1 as a circular region of radius $3'.5$ centered at $24'$ east from SS433, and w1 a circle of radius $3'.75$ centered at $19'$ west. These translate into parameter (z_s, z_f) as $(32\,\mathrm{pc}, 44\,\mathrm{pc})$ for e1 and $(24\,\mathrm{pc}, 36\,\mathrm{pc})$ for w1 in Equation (19). We note that the *XMM-Newton* data used in Abeysekara et al. (2018) are taken from a slightly larger region (a circle of $6'$ radius centered at e1), which we do not take into account here. As we consider the emission from a region that spans approximately 10 pc across, we do not expect any influence from the orbital or precession phase, which may appear only on a significantly smaller scales.
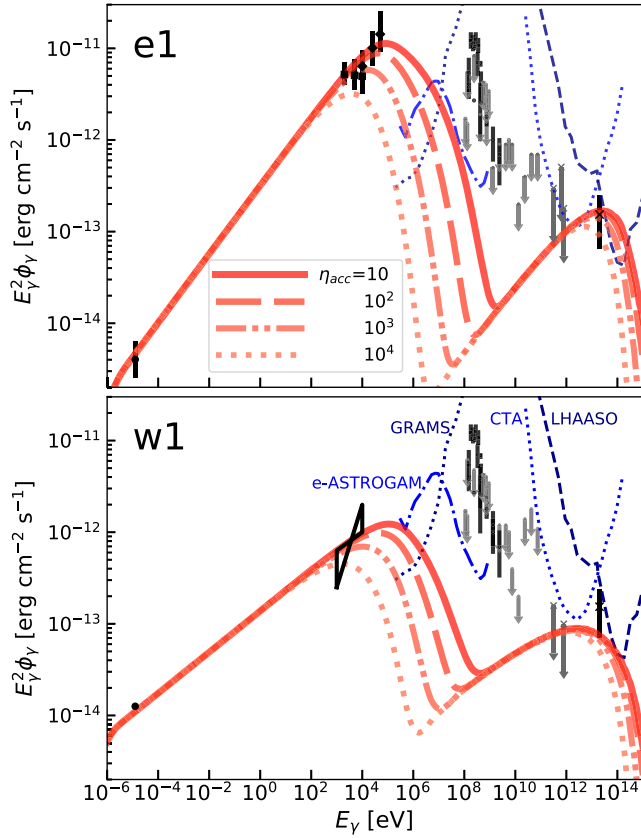
Figure 2. Broadband spectral energy distribution of the e1 (top) and w1 (bottom) region. Orange curves are model predictions for different choices of $\eta_{\rm acc}$, as labeled. Black and gray points are observational data and upper limits, respectively, from Geldzahler et al. (1980) (radio), Brinkmann et al. (2007), Safi-Harb & Ögelman (1997), Safi-Harb & Petre (1999) (X-ray), Bordas et al. (2017), Xing et al. (2019), Rasul et al. (2019), Sun et al. (2019) (HE), Ahnen et al. (2018), Kar (2017), Abeysekara et al. (2018) (VHE). Expected sensitivities are also shown for CTA (North, 50 hours; Acharya et al. 2019), LHAASO (one year; Bai et al. 2019), e-ASTROGAM (three years; De Angelis et al. 2017), and GRAMS (three years; Aramaki et al. 2020).

4. Nonthermal Leptonic Emission from Knots in SS433 Jets

In Figure 2, we show the spectral energy distribution for the e1 and w1 region. Our leptonic models explain the radio, X-ray, and VHE data. For the GeV data, our predictions in the HE regime are far below the data for both regions. This indicates that it is difficult to explain the GeV data simultaneously with other wavelength data in the framework of our leptonic models from knot regions. Thus, most GeV photons should be produced in different regions or by different mechanisms.

In Table 1, we list the required parameters for the fit. The slope $p_{\rm inj}$ is determined from the radio and X-ray data, while L_B and L_e are derived by combining them with the HAWC data. The derived magnetic field strengths are 16 and 9 μG for e1 and w1, respectively.

The mechanism responsible for the maximum energy cannot be determined from this fit. We temporarily focus on the case where it is limited by synchrotron losses (Equation (10)). Then, the magnetic field and acceleration efficiency, $\eta_{\rm acc}$, define the

Table 1
Model Parameters

Region	$p_{\rm inj}$	L_e [10^{39} erg s^{-1}]	L_B [10^{39} erg s^{-1}]
e1	2.25	0.02	0.18
w1	2.55	0.08	0.06

maximum electron energy:

$$E_{e,\max}^{\rm syn} = 1.5~{\rm PeV}\left(\frac{\eta_{\rm acc}}{10^2}\right)^{-\frac{1}{2}}\left(\frac{B}{16~\mu{\rm G}}\right)^{-\frac{1}{2}}. \qquad (26)$$

In our model, the hard X-ray data require $\eta_{\rm acc} \lesssim 10^2$ for both regions. Although our model does not specify the acceleration processes, it would be helpful to interpret $\eta_{\rm acc}$ in the framework of two representative scenarios. First, we consider diffusive shock acceleration. In this mechanism, particles gain energy as they cycle upstream and downstream across the shock front. The acceleration timescale in a parallel shock is given by $\tau_{\rm acc}^{\rm DSA} \simeq 10D/v_{\rm sh}^2$ (e.g., Bell 2013). This translates into the efficiency in Equation (5) as

$$\eta_{\rm acc}^{\rm DSA} \simeq \frac{10\eta_g}{3(v_{\rm sh}/c)^2} \simeq 10^2\left(\frac{\eta_g}{2}\right)\left(\frac{v_{\rm sh}}{0.26c}\right)^{-2}. \qquad (27)$$

Thus, our results suggest that the diffusion coefficient may satisfy $\eta_g \lesssim 2$, indicating strong particle confinement close to the Bohm limit. Such a high particle acceleration efficiency is known to be achieved in young supernova remnants (e.g., Stage et al. 2006; Uchiyama et al. 2007; Tsuji et al. 2019), while it is thought to be much more inefficient in extragalactic black hole jets (e.g., Araudo et al. 2015; Inoue & Tanaka 2016; Tanada et al. 2019), possibly due to the inefficiency of the diffusive shock acceleration mechanism in the relativistic regime (Bell et al. 2018).

Second, we consider the stochastic acceleration. In this mechanism, particles gain energy as they are resonantly scattered by magnetohydrodynamic turbulence (e.g., Dermer & Menon 2009). Assuming that the smallest turbulence wavenumber is equal to R^{-1}, the timescale for acceleration is given by

$$\tau_{\rm acc}^{\rm S} \simeq \frac{1}{\kappa_{\rm B}}\left(\frac{v_A}{c}\right)^{-2}\left(\frac{r_L}{R}\right)^{2-q}\tau_{\rm dyn}, \qquad (28)$$

where $\kappa_{\rm B}$ is the ratio of the strength of turbulent field compared to the background field, $\tau_{\rm dyn} = R/c$ is the dynamical timescale and q describes the spectrum of the turbulence. This expression is derived under quasi-linear approximation ($\kappa_{\rm B} \ll 1$), but has a wider applicability (O'Sullivan et al. 2009). The Alfvén velocity $v_A = B/\sqrt{4\pi m_p n_p}$ can be expressed in the form of

$$\frac{v_A}{c} = \sqrt{\frac{L_B}{\Gamma \dot{M}c^2}} \qquad (29)$$

Combining the above equations and assuming the Kolmogorov-type spectrum ($q = 5/3$), we have

$$\eta_{\rm acc}^{\rm S} \simeq \frac{10^3}{\kappa_{\rm B}}\left(\frac{\dot{M}}{10^{-7}M_\odot~{\rm yr}^{-1}}\right)\left(\frac{L_B}{10^{38}~{\rm erg~s}^{-1}}\right)^{-1}. \qquad (30)$$

for $R = 6$ pc and $E = 1$ PeV. Thus, the stochastic acceleration is likely insufficient to reach the high efficiency of $\eta_{\rm acc} < 10^2$,

though it is not firmly ruled out due to simplifications in this estimate.

So far, we have focused on the case where electron energy is limited by the synchrotron loss. If escape is efficient, the confinement limit should be dominant for electrons when $E_{e,\max}^{\mathrm{con}} < E_{e,\max}^{\mathrm{syn}}$, or,

$$\eta_g > 20 \left(\frac{R}{6\ \mathrm{pc}}\right)^2 \left(\frac{B}{16\ \mu\mathrm{G}}\right)^3. \tag{31}$$

In this case, our results constrain the product $\eta_{\mathrm{acc}}\eta_g$ to $\eta_{\mathrm{acc}}\eta_g \lesssim 10^3$. Combining this with Equation (31), we obtain $\eta_{\mathrm{acc}} \lesssim 10^2$.

The acceleration of leptons may imply the presence of nonthermal protons because they have a larger Larmor radius and are more easily injected into the acceleration processes. Synchrotron losses are inefficient for protons, and the maximum energy is limited by confinement:

$$E_{p,\max}^{\mathrm{con}} = 5\ \mathrm{PeV}\left(\frac{\eta_{\mathrm{acc}}\eta_g}{10^2}\right)^{-\frac{1}{2}}\left(\frac{L_{\mathrm{B}}}{10^{38}\ \mathrm{erg\ s}^{-1}}\right)^{\frac{1}{2}}. \tag{32}$$

If we assume that the same acceleration process is at work both for electrons and protons, we can apply the same value of η_{acc}. Then, the constraint $\eta_{\mathrm{acc}} \lesssim 10^2$ formally suggests that SS433 can accelerate protons beyond a PeV, if the Bohm factor η_g is sufficiently small.

As noted in Section 3.2, the radio flux may be dominated by other components. If we treat the radio data as upper limits, the parameter p_{inj} can become as small as 1.9. The spectral turnover and cutoff predicted in our model and constraints on η_{acc} remain unchanged because they are derived from the hard X-ray data and determined by the timescales of synchrotron cooling τ_{syn} and transport τ_{adv}.

4.1. Comparison with Previous Studies

We now compare our results with other recent studies. Our model spectra are significantly different from results by Abeysekara et al. (2018, e1) and Xing et al. (2019, w1). They require a hard spectrum of $p_{\mathrm{inj}} = 1.9$ for electrons, while we derive $p_{\mathrm{inj}} = 2.25$ and 2.55 for e1 and w1, respectively. The main differences are twofold. First, they calculate the evolution of particles assuming continuous injection throughout the source lifetime, for which they adopted $t_{\mathrm{lifetime}} \simeq 30$ kyr. Thus, their spectra show cooling breaks in the electron spectra at $E_e = 2\ (B/16\ \mu\mathrm{G})^{-2}(t_{\mathrm{lifetime}}/30\ \mathrm{kyr})^{-1}$ TeV, and require a hard p_{inj}. In contrast, we integrate the particle spectrum from z_s and z_f (Equation (19)), and the effective lifetime is set by $\tau_{\mathrm{adv}} \simeq (z_f - z_s)/v_z \simeq 150$ yr. Second, while they only include radiative losses, we also consider adiabatic loss. In Figure 3, we compare energy loss timescales for different processes. Adiabatic losses dominate below 100 TeV, significantly limiting the total electron energy. Note that we employ a simple case of a conical jet to evaluate the adiabatic loss. The jets may be collimated by surrounding material and keep nearly cylindrical ($\partial R/\partial z = 0$), experiencing no adiabatic loss. In our calculation, As the effect of particle transport is dominant over that of adiabatic cooling ($\tau_{\mathrm{adv}} < \tau_{\mathrm{ad}}$), the results remain unchanged for different modeling of jet expansion, as long as we focus on the emission from the synchrotron knots.
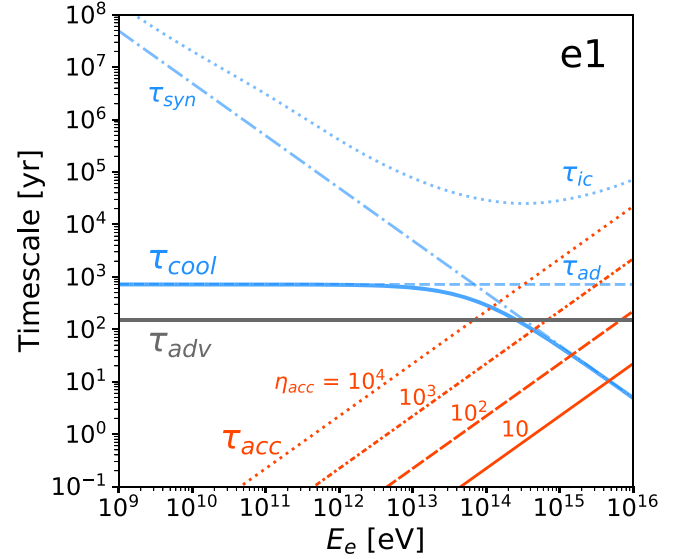
Figure 3. Cooling timescales ($\tau = \gamma/|\dot{\gamma}|$) for different processes for the e1 region, as marked. For comparison, timescales of confinement and acceleration are also shown.

4.2. Prospects for Future Observations

We examine expectations for future observations. The hard X-ray (10–100 keV) observations will be most critical. *NuSTAR* can provide a better determination of the spectrum from both regions in this regime. In the MeV–GeV band, planned telescopes such as *GRAMS* (Aramaki et al. 2020), *e-ASTROGAM* (De Angelis et al. 2017), and AMEGO (McEnery et al. 2019) will be able to study the highest-energy synchrotron photons, though the localization of emitting region would be difficult for their expected angular resolutions. Our models predict that these observations would detect spectral turnover and cutoff (Figure 2), placing strong constraints on physical properties and acceleration processes. In the VHE regime, our results indicate that CTA and LHAASO observations might be able to detect gamma rays from both regions (Acharya et al. 2019; Bai et al. 2019).

5. Morphology of Emission Regions

The location of emission sites is an important ingredient in our model. In this section, we examine explanations for the size of X-ray knots and briefly discuss uncertainties due to different morphology of the X-ray and IC emission.

5.1. X-Ray Knot Size in SS433 Jets

The X-ray images in the ~ 1–10 keV range show a clear feature of knots with a size comparable with the e1 region, $s^{\mathrm{X}} \simeq 5$–10 pc (Safi-Harb & Ögelman 1997). The typical energy of electrons responsible for the X-ray emission at 1 keV is 30 $(B/15\ \mu\mathrm{G})^{-1/2}$ TeV, and the synchrotron cooling time for these electrons is 1.5 $(B/15\ \mu\mathrm{G})^{-3/2}$ kyr. The advection length during that is

$$s_{\mathrm{syn}}^{\mathrm{X}} = 120\left(\frac{B}{15\ \mu\mathrm{G}}\right)^{-\frac{3}{2}}\left(\frac{v_z}{0.26c}\right)\ \mathrm{pc}. \tag{33}$$

Thus, with our standard value of $v_z = 0.26c$, the X-ray knot size cannot be explained by the synchrotron cooling. Below,

we will examine several possible physical processes that may determine the X-ray knot size.

Synchrotron cooling: unlikely. The knot length may be explained by the synchrotron cooling if we adopt a velocity smaller than $0.26c$, but the spectrum places tight constraints; the emitting particles should be in the fast cooling regime, where photon spectrum would be $\Gamma_{\rm ph} = 2$ (for an E_e^{-2} injection). This contradicts with the hard X-ray spectrum of $\Gamma_{\rm ph} \simeq 1.5$. Thus, synchrotron cooling cannot be responsible for determining the X-ray knot size, unless the electrons are injected with an extremely hard spectrum of $\simeq E_e^{-1}$.

Adiabatic cooling: possible for a nonconical jet. If the jet is conical, the adiabatic cooling operates on a scale of the jet length, and the knot size would be $s_{\rm ad} \simeq 3z/2 \simeq 60$ pc, much larger than observed. However, it may experience local expansion or compression due to the pressure from the surrounding material, producing standing coherent waves (called the Mach disk) or more complicated hydrodynamical structures. If the jet has a structure that enhances the adiabatic cooling rate locally, the X-ray knot size could be explained.

Enhanced magnetic field: possible. The magnetic field in the jets may not be distributed uniformly, but have local amplifications probably due to the local compression of the jet or plasma instabilities. The size of the X-ray knot may correspond to the region with an enhanced magnetic field, probably due to turbulence.

Very recent acceleration: unlikely. There is a theoretical possibility that acceleration has started very recently, Δt years ago, and advection determines the size of knots. We cannot rule out the possibility that Δt is close to $\tau_{\rm adv}$, but this requires a coincidence. There could also be a possibility that the acceleration takes place in an extended region, rather than at a specific location in the jet, and $\Delta t \ll \tau_{\rm adv}$. However, if this is the case, the injection power required to produce the observed X-ray luminosity would be much larger than in other scenarios. The dissipation of such a large amount of power would have to produce much brighter thermal bremsstrahlung emission from the heated plasma, which is not observed. Thus, this scenario is unlikely.

Future X-ray observations with high angular resolution would be important to distinguish these scenarios. If the knot size is defined by the adiabatic cooling, we should see no dependence on the photon energies. If the knot size corresponds to the size of the region where the magnetic field is enhanced due to turbulence, we expect patchy bright emission inside the emitting region due to the inhomogeneity of magnetic field strength.

5.2. IC Emitter Size in SS433 Jets

The size of gamma-ray emitting regions, $s^{\rm VHE}$, is not yet clear. The gamma rays with an energy of 25 TeV are predominately generated on the cosmic microwave background, and the emitting electrons have an energy of 100 TeV. The synchrotron cooling time is $0.5 \, (B/15 \, \mu{\rm G})^{-3/2}$ kyr, during which these electrons are advected to a distance of

$$s_{\rm syn}^{\rm VHE} = 40 \left(\frac{B}{15 \, \mu{\rm G}} \right)^{-\frac{3}{2}} \left(\frac{v_z}{0.26c} \right) {\rm pc}. \quad (34)$$

Adiabatic losses may produce a comparable advection distance for a conical jet, or smaller distance if they are locally

enhanced. In any case, the IC emitter is likely larger than X-ray knots.

The difference between $s^{\rm VHE}$ and $s^{\rm X}$ can induce uncertainties in our calculation. In particular, though we have used the observed VHE flux to derive physical parameter for the e1 and w1 regions, the real TeV flux from these two knots are likely smaller, provided that $s^{\rm VHE} > s^{\rm X}$. This should primarily affect the estimate on B. Because the dominant target for IC scattering is provided by the diffuse background, synchrotron, and IC luminosities relate as $L_{\rm syn}/L_{\rm ic} \propto B^2$, thus the magnetic field strength may be larger approximately by a factor of $\sqrt{s^{\rm VHE}/s^{\rm X}}$ when we take the size of emitting regions into account. Future CTA observations would better constrain the size of the IC emitter with its unparalleled angular resolution.

6. Limitations

In this section, we examine limitations of our model and their impact on our results.

6.1. Acceleration Site

We have focused on the case where $z_{\rm acc} = z_s$, but in principle they could be different. If $z_{\rm acc} \ll z_s$, we should take into account the particle cooling between $z_{\rm acc}$ and z_s. In such a situation, the magnetic field at the acceleration site, $B_{\rm acc}$, can also be different from the field at the emission region, $B_{\rm emit}$, which is derived by the spectral fitting. This difference would change our upper limits on $\eta_{\rm acc}$ by a factor of $B_{\rm emit}/B_{\rm acc}$ (see Equation (10)). In particular, $B_{\rm acc}$ could be smaller than $B_{\rm emit}$ otherwise we should see brighter synchrotron emission from the acceleration site. If this is the case, future observations should reveal fainter synchrotron emission from the acceleration site, placing better constraints on the magnetic field there. The difference between $B_{\rm acc}$ and $B_{\rm emit}$ might be the reason why shocks are not yet resolved (Abeysekara et al. 2018).

6.2. Velocity in the Knot Region

In our calculation, we have used $v_z = 0.26c$, which is determined at the jet base (Margon & Anderson 1989; Eikenberry et al. 2001). The bulk velocity in the knot region is less certain from observations, but possibly be smaller than $0.26c$ because knots are located at large distances from the core (Goodall et al. 2011a, 2011b; Monceau-Baroux et al. 2014, 2015; Panferov 2014, 2017; Bowler & Keppens 2018). The primarily effect of adopting a smaller bulk velocity would be flattening of the spectrum, because the transition from advection-dominated regime to fast cooling regime would occur at lower energy. This would produce a flat ($\Gamma_{\rm ph} \simeq 2$) X-ray spectrum before a cutoff. In addition, the estimate on the size of the emitting regions would be proportionally changed for a different jet velocity. In other words, a better determination of both the spectrum and morphology in X-ray bands would be critical to constrain the bulk velocity in the knot region.

7. Conclusions

Multiwavelength observations of the microquasar SS433 offer the potential for detailed studies on particle acceleration in astrophysical jets. In this paper, we first present a theoretical foundation to interpret nonthermal emission from astrophysical jets quantitatively. We then consider leptonic emission from the

X-ray knots in SS433's jets. We use the same data sets as in Abeysekara et al. ([2018](#)) and Xing et al. ([2019](#)), but treat the particle transport and evolution in the jet in more detail, and produce substantially different predictions.

Our analysis produced three main results. First, leptonic models can explain the radio, X-ray, and VHE gamma-ray data for both the e1 and w1 regions. However, the GeV data remain unexplained for any reasonable parameter set, which indicates that they are mostly from different regions or mechanisms. Second, the efficiency of particle acceleration should be very high, $\eta_{\rm acc} \lesssim 10^2$, to explain the X-ray and TeV gamma-ray data. This could be realized by the diffusive shock acceleration, for a strong confinement case close to the Bohm limit, $\eta_g \sim 1$. Such high efficiency of particle acceleration may imply that SS433 jets can also accelerate protons beyond a PeV. Third, future X-ray/MeV observations would be most critical to constrain models and better understand the acceleration processes. In particular, our models predict a spectral turnover and cutoff in this energy band.

We note that our models have broader implications that can be studied by future observations.

1. We have focused on the emission from e1 and w1 throughout this work. Our model can also predict emission from different regions by changing the parameter z_s and z_f in Equation ([19](#)), provided that there is no effect of reacceleration. As sketched in Figure [1](#) and explained in Section [2.5](#) , in regions farther away from the binary, the synchrotron emission has spectral break steeper than expected from the cooling break. Interestingly, a hint of such a steep break is seen from observations of e2 and w2 regions (Safi-Harb & Ögelman [1997](#)). A better determination of the X-ray spectrum in these regions is the key to test this prediction.

2. We have focused on leptonic emission throughout this work. If protons are also accelerated in the jets, they may interact with the ambient medium to produce pionic gamma rays. As the cooling time for protons, $\tau_{\rm pp}$, is long, we may see emission from protons accumulated during the lifetime of SS433's jets, which should extend over much a larger region than X-ray knots. The jet kinetic power $\sim 10^{39}$ erg s^{-1} and system age ~ 20 kyr suggest that the jet has released the total energy of $E_{\rm jet} \sim 10^{51}$ erg. Assuming that 10% of this goes to nonthermal protons between 1 GeV and 1 PeV, and for an E_p^{-2} injection spectrum, the proton energy would be $0.1 E_{\rm jet}/\ln(10^6)$, yielding a TeV gamma-ray luminosity of $\sim 0.1 E_{\rm jet}/(3\tau_{pp}\ln(10^6))$. Thus, we could expect TeV gamma-ray flux of

$$F_\gamma \sim 10^{-13}(n_{\rm gas}/0.2\ {\rm cm}^{-3})\ {\rm erg\ s}^{-1}\ {\rm cm}^{-2}. \quad (35)$$
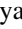
This could suggest that the hadronic gamma rays from the W50/SS433 system could also be detected at CTA and LHAASO. Furthermore, they may contribute to the VHE flux detected by HAWC, though it requires strong confinement of protons close to the emitting regions.

The first detection of SS433 in the VHE regime has increased excitement in gamma-ray astronomy, by adding microquasars to a growing class of TeV sources. Our work highlights their importance as Galactic particle accelerators. Future observations with X-ray and VHE gamma rays of SS433 and other microquasars should shed new light into our understanding of the HE sky.

ORCID iDs

Takahiro Sudoh ⬤ https://orcid.org/0000-0002-6884-1733
Yoshiyuki Inoue ⬤ https://orcid.org/0000-0002-7272-1136
Dmitry Khangulyan ⬤ https://orcid.org/0000-0002-7576-7869

References

Abell, G. O., & Margon, B. 1979, Natur, 279, 701
Abeysekara, A. U., Albert, A., Alfaro, R., et al. 2018, Natur, 562, 82
Acharya, B. S., Agudo, I., Al Samarai, I., et al. 2019, Science with the Cherenkov Telescope Array (World Scientific Publishing Co.: Singapore)
Aharonian, F. A., Atoyan, A. M., & Kifune, T. 1997, MNRAS, 291, 162
Aharonian, F. A., Kelner, S. R., & Prosekin, A. Y. 2010, PhRvD, 82, 043002
Ahnen, M. L., Ansoldi, S., Antonelli, L. A., et al. 2018, A&A, 612, A14
Amano, T., & Hoshino, M. 2012, ASSP, 33, 143
Antokhina, E. A., & Cherepashchuk, A. M. 1987, SvA, 31, 295
Aramaki, T., Adrian, P. O. H., Karagiorgi, G., & Odaka, H. 2020, APh, 114, 107
Araudo, A. T., Bell, A. R., & Blundell, K. M. 2015, ApJ, 806, 243
Atoyan, A. M., & Aharonian, F. A. 1999, MNRAS, 302, 253
Bai, X., Bi, B. Y., Bi, X. J., et al. 2019, arXiv:1905.02773
Begelman, M. C., King, A. R., & Pringle, J. E. 2006, MNRAS, 370, 399
Bell, A. R. 2013, APh, 43, 56
Bell, A. R., Araudo, A. T., Matthews, J. H., & Blundell, K. M. 2018, MNRAS, 473, 2364
Blumenthal, G. R., & Gould, R. J. 1970, RvMP, 42, 237
Blundell, K. M., & Bowler, M. G. 2004, ApJL, 616, L159
Bordas, P., Bosch-Ramon, V., Paredes, J. M., & Perucho, M. 2009, A&A, 497, 325
Bordas, P., Sun, X., Yang, R., Kafexhiu, E., & Aharonian, F. A. 2017, AIP Conf. Proc. in 6th Int. Symp. on High Energy Gamma-Ray Astronomy (Melville, NY: AIP)
Bordas, P., Yang, R., Kafexhiu, E., & Aharonian, F. 2015, ApJL, 807, L8
Bosch-Ramon, V., Romero, G. E., & Paredes, J. M. 2006, A&A, 447, 263
Bowler, M. G., & Keppens, R. 2018, A&A, 617, A29
Brinkmann, W., Aschenbach, B., & Kawai, N. 1996, A&A, 312, 306
Brinkmann, W., & Kawai, N. 2000, A&A, 363, 640
Brinkmann, W., Kotani, T., & Kawai, N. 2005, A&A, 431, 575
Brinkmann, W., Pratt, G. W., Rohr, S., Kawai, N., & Burwitz, V. 2007, A&A, 463, 611
Broderick, J. W., Fender, R. P., Miller-Jones, J. C. A., et al. 2018, MNRAS, 475, 5360
Bykov, A. M., Pavlov, G. G., Artemyev, A. V., & Uvarov, Y. A. 2012, MNRAS, 421, L67
Cherepashchuk, A. M., Postnov, K. A., & Belinski, A. A. 2019, MNRAS, 485, 2638
Cherepashchuk, A. M., Sunyaev, R. A., Molkov, S. V., et al. 2013, MNRAS, 436, 2004
De Angelis, A., Tatischeff, V., Tavani, M., et al. 2017, ExA, 44, 25

Derishev, E., & Aharonian, F. 2019, ApJ, 887, 181
Dermer, C. D., & Menon, G. 2009, High Energy Radiation from Black Holes
    (Princeton, NJ: Princeton Univ. Press)
Downes, A. J. B., Pauls, T., & Salter, C. J. 1986, MNRAS, 218, 393
Dubner, G. M., Holdaway, M., Goss, W. M., & Mirabel, I. F. 1998, AJ,
    116, 1842
Eikenberry, S. S., Cameron, P. B., Fierce, B. W., et al. 2001, ApJ, 561, 1027
Fabian, A. C., & Rees, M. J. 1979, MNRAS, 187, 13P
Fabrika, S. 2004, ASPRv, 12, 1
Geldzahler, B. J., Pauls, T., & Salter, C. J. 1980, A&A, 84, 237
Goodall, P. T., Alouani-Bibi, F., & Blundell, K. M. 2011a, MNRAS, 414, 2838
Goodall, P. T., Blundell, K. M., & Bell Burnell, S. J. 2011b, MNRAS,
    414, 2828
Green, D. A. 2004, BASI, 32, 335
Gupta, S., Böttcher, M., & Dermer, C. D. 2006, ApJ, 644, 409
Heinz, S., & Sunyaev, R. 2002, A&A, 390, 751
Hillas, A. M. 1984, ARA&A, 22, 425
Hillwig, T. C., & Gies, D. R. 2008, ApJL, 676, L37
Hillwig, T. C., Gies, D. R., Huang, W., et al. 2004, ApJ, 615, 422
Hunter, J. D. 2007, CSE, 9, 90
Inoue, Y., & Tanaka, Y. T. 2016, ApJ, 828, 13
Kar, P. 2017, ICRC, 35, 713
Kelner, S. R., Aharonian, F. A., & Khangulyan, D. 2013, ApJ, 774, 61
Khangulyan, D., Aharonian, F. A., & Kelner, S. R. 2014, ApJ, 783, 100
Khangulyan, D., Bosch-Ramon, V., & Uchiyama, Y. 2018, MNRAS,
    481, 1455
Kotani, T., Kawai, N., Matsuoka, M., & Brinkmann, W. 1996, PASJ, 48, 619
Kubota, K., Ueda, Y., Fabrika, S., et al. 2010, ApJ, 709, 1374
Lockman, F. J., Blundell, K. M., & Goss, W. M. 2007, MNRAS, 381, 881
Margon, B., & Anderson, S. F. 1989, ApJ, 347, 448
Marshall, H. L., Canizares, C. R., & Schulz, N. S. 2002, ApJ, 564, 941
McEnery, J., Abel Barrio, J., Agudo, I., et al. 2019, arXiv:1907.07558
Medvedev, A., & Fabrika, S. 2010, MNRAS, 402, 479
Molina, E., & Bosch-Ramon, V. 2018, A&A, 618, A146
Monceau-Baroux, R., Porth, O., Meliani, Z., & Keppens, R. 2014, A&A,
    561, A30
Monceau-Baroux, R., Porth, O., Meliani, Z., & Keppens, R. 2015, A&A,
    574, A143
Oliphant, T. 2006, NumPy: A Guide to NumPy, http://www.numpy.org/
    (Trelgol Publishing)
Orellana, M., Bordas, P., Bosch-Ramon, V., Romero, G. E., & Paredes, J. M.
    2007, A&A, 476, 9
O'Sullivan, S., Reville, B., & Taylor, A. M. 2009, MNRAS, 400, 248
Panferov, A. 2014, A&A, 562, A130
Panferov, A. A. 2017, A&A, 599, A77
Pauli, V., Gommers, R., Oliphant, T.E., et al. 2019, arXiv:1907.10121
Pepe, C., Vila, G. S., & Romero, G. E. 2015, A&A, 584, A95
Perucho, M., & Bosch-Ramon, V. 2008, A&A, 482, 917
Popescu, C. C., Yang, R., Tuffs, R. J., et al. 2017, MNRAS, 470, 2539
Porter, T. A., Jóhannesson, G., & Moskalenko, I. V. 2017, ApJ, 846, 67
Rasul, K., Chadwick, P. M., Graham, J. A., & Brown, A. M. 2019, MNRAS,
    485, 2970
Reynoso, M. M., & Carulli, A. M. 2019, APh, 109, 25
Reynoso, M. M., Romero, G. E., & Christiansen, H. R. 2008, MNRAS,
    387, 1745
Romero, G. E., Torres, D. F., Kaufman Bernadó, M. M., & Mirabel, I. F. 2003,
    A&A, 410, L1
Romero, G. E., & Vila, G. S. 2008, A&A, 485, 623
Safi-Harb, S., & Ögelman, H. 1997, ApJ, 483, 868
Safi-Harb, S., & Petre, R. 1999, ApJ, 512, 784
Stage, M. D., Allen, G. E., Houck, J. C., & Davis, J. E. 2006, NatPh, 2, 614
Sun, X.-N., Yang, R.-Z., Liu, B., Xi, S.-Q., & Wang, X.-Y. 2019, A&A,
    626, A113
Tanada, K., Kataoka, J., & Inoue, Y. 2019, ApJ, 878, 139
Tsuji, N., Uchiyama, Y., Aharonian, F., et al. 2019, ApJ, 877, 96
Uchiyama, Y., Aharonian, F. A., Tanaka, T., Takahashi, T., & Maeda, Y. 2007,
    Natur, 449, 576
Vaidya, B., Mignone, A., Bodo, G., Rossi, P., & Massaglia, S. 2018, ApJ,
    865, 144
van der Walt, S., Colbert, S. C., & Varoquaux, G. 2011, CSE, 13, 22
Vila, G. S., & Romero, G. E. 2010, MNRAS, 403, 1457
Waisberg, I., Dexter, J., Olivier-Petrucci, P., Dubus, G., & Perraut, K. 2019,
    A&A, 624, A127
Watson, M. G., Willingale, R., Grindlay, J. E., & Seward, F. D. 1983, ApJ,
    273, 688
Webb, G. M. 1989, ApJ, 340, 1112
Xing, Y., Wang, Z., Zhang, X., Chen, Y., & Jithesh, V. 2019, ApJ, 872, 25
Yamauchi, S., Kawai, N., & Aoki, T. 1994, PASJ, 46, L109
Zdziarski, A. A., Pjanka, P., Sikora, M., & Stawarz, Ł. 2014, MNRAS,
    442, 3243
Zealey, W. J., Dopita, M. A., & Malin, D. F. 1980, MNRAS, 192, 731
Zhang, J.-F., Li, Z.-R., Xiang, F.-Y., & Lu, J.-F. 2018, MNRAS, 473, 3211